Journal of Materials Chemistry C

PAPER

View Article Online
View Journal | View Issue

Cite this: J. Mater. Chem. C, 2017, 5, 10509

Determination of Schottky barrier height and enhanced photoelectron generation in novel plasmonic immobilized multisegmented (Au/TiO_2) nanorod arrays (NRAs) suitable for solar energy conversion applications†

Muhammad Shahid Arshad, *[a] Špela Trafela, [b] Kristina Žužek Rožman, [b] Janez Kovač,[c] Petar Djinović [a] and Albin Pintar[a]

For the past several years, different strategies have been developed to design and fabricate Au/TiO_2 nanostructures for solar-light-driven applications. Owing to the localized surface plasmon resonance properties of Au, Au/TiO_2 nanostructures display extraordinary features including enhanced visible light harvesting, hot electron injection, and Schottky barriers to minimize back electron transfer; these factors maximize device performance. In this report, novel free-standing immobilized TiO_2 and multisegmented Au/TiO_2 nanorod arrays (NRAs) were successfully fabricated with a template-assisted electrodeposition technique to examine several physical phenomena like the Schottky barrier height (SBH), photoelectron generation, as well as the mechanism of hot electron transfer. Pristine TiO_2 NRAs exhibit amorphous behaviour with strong absorption under UV-light; however, for Au/TiO_2 NRAs, transverse and longitudinal plasmon modes were observed under visible light, which correlates closely with our theoretical predictions. The reduced binding energy of Au $4f_{7/2}$ and concurrent increase in the Ti^{3+}–O species observed with X-ray photoelectron spectroscopy (XPS) is direct evidence for charge transfer from oxygen vacancies in TiO_2 to Au segments. XPS analysis on valence band maxima (VBM) helps us to determine an SBH of 0.23 eV at the interface between the Au and TiO_2 segments. The low value of SBH is attributed to the high density of oxygen vacancies in TiO_2 due to the amorphous structure, and is very close to the theoretical literature value. Photoelectrochemical (PEC) measurements showed 4× improved photoelectron generation in Au/TiO_2 NRAs in comparison to pristine TiO_2 NRAs. This improvement is attributed to the hot electron injection, plasmonic resonance energy transfer (PRET) and efficient charge separation and migration due to the small SBH at the interface of Au and TiO_2. Our results concluded that novel immobilized multisegmented (Au/TiO_2) NRAs have great potential for solar-light-driven applications.

Received 13th June 2017,
Accepted 8th August 2017

DOI: 10.1039/c7tc02633a

rsc.li/materials-c

Introduction

Plasmonic metals (Au, Ag) have extremely large absorption/scattering cross-sections in the visible range and the ability to strongly focus light close to their surface. Therefore, they can offer new opportunities to overcome the limited efficiency of TiO_2 for utilizing it in various solar conversion devices such as photocatalysts and photovoltaic cells.[1] The underlying physical phenomenon for improved visible light interaction is based on surface plasmon resonance (SPR). SPR helps in generating electrons and holes in the following fashion: it has been widely recognized that the hot electrons originate from the decay of SPR and can be injected into the conduction band of TiO_2, known as the hot electron injection process.[2] Thus, combining

[a] Department for Environmental Sciences and Engineering, National Institute of Chemistry, Hajdrihova 19, SI-1001 Ljubljana, Slovenia. E-mail: shahid.arshad@ki.si
[b] Department for Nanostructured Materials, Jožef Stefan Institute, Jamova 39, SI-1000 Ljubljana, Slovenia
[c] Department of Surface Engineering and Optoelectronics, Jožef Stefan Institute, Jamova 39, SI-1000 Ljubljana, Slovenia

† Electronic supplementary information (ESI) available: Fig. S1: (a) The extinction spectra of Au NRs with various AR. (b) Linear relationships between λ_{max} and AR for Au NRs. Fig. S2: The extinction spectra of Au and multisegmented Au/TiO_2 NR with the same AR. Fig. S3: (a) Hexagonally arranged 7 NRAs separated by distance (S) with diameter (D). (b) Extinction spectra of a single Au NR and Au NRs in arrays with different separations (S = 15 and 20 nm). NFE of hexagonally arranged Au NRAs with separation of around (c) 15 nm and (d) 20 nm. Fig. S4: XPS survey spectrum of TiO_2 and Au/TiO_2 NRAs. See DOI: 10.1039/c7tc02633a

the plasmonic metals with TiO_2 can enhance the light interaction of TiO_2 through scattering, absorption, sensitization and hot electron injection.[3] The plasmonic metals not only improve the photoabsorption *via* SPR, but also provide a Schottky barrier (SB) at the interface between the metal and the semiconductor. This SB can provide excellent charge separation in such nanostructures. The Schottky barrier height (SBH) has been suggested to be an important parameter influencing the efficiency of the plasmon-induced electron injection at the metal/semiconductor interfaces.[4] Despite the significance of SBH, there are only a few experimental reports on this topic. Therefore, in-depth understanding about SBH is necessary and could help in improving the plasmon-driven hot-carrier transfer between metal and semiconductor, which significantly affects the overall photocatalytic activity. X-ray photoelectron spectroscopy (XPS) is widely used and is considered the most efficient characterization technique for the determination of SBH.[5–7]

Conventional planar configurations (*e.g.* thin films) have promoted the efficiency of energy-conversion devices close to theoretical values.[8] One promising strategy to further improve the performance is to construct free standing immobilized 1D nanostructure arrays.[8] So far, various techniques have been used for the fabrication of multisegmented heterogeneous 1D nanostructure arrays.[9–12] Among these techniques, hard nanoporous templates provide a straightforward scaffold for the fabrication of 1D nanostructure arrays of different materials. The interface between multiple components and the morphological parameters (length and diameter) can also be engineered *via* varying the deposition parameters, qualifying it as an appropriate method to fabricate complicated multisegmented heterojunction 1D nanostructures.[8]

Herein, we have fabricated novel multisegmented Au/TiO_2 NRAs as a representative example for investigating the harvesting of visible light, determination of SBH, and enhancement in photoelectron generation. Although metal/semiconductor photocatalysts have been widely employed in photocatalytic reactions, the SBH between amorphous TiO_2 and Au, hot electron injection and plasmonic resonance energy transfer (PRET) phenomena from Au to TiO_2 is less understood. A few key features in the novel multisegmented Au/TiO_2 NRAs are described below:

(1) Immobilized free standing multisegmented Au/TiO_2 NRAs provide strong light interaction due to the large surface available for interacting with photons, thus facilitating higher photoabsorption.

(2) The proposed elongated shape of Au segments is expected to increase vectoral electron transfer onto the TiO_2 surface.

(3) Au/TiO_2 NRAs combine the advantages of different materials. For instance, TiO_2 absorbs UV light, however, Au is active in the visible light range due to the SPR effect, thus resulting in significant improvement in photoelectron generation.

(4) A direct interface without surfactants and band alignment between TiO_2 and Au significantly improve the hot electron injections and PRET enhancement from Au to TiO_2. Due to the formation of SBH at the interface, there is efficient charge separation, which suppresses e^-–h^+ recombination events.

We report on the realization of novel free-standing immobilized multisegmented Au/TiO_2 nanorod arrays (NRAs) through the template-assisted electrodeposition technique. TiO_2 is a widely studied semiconductor with promising photocatalytic, photovoltaic, and biomedical applications. Au segments have been incorporated to enhance and broaden the light utilization of TiO_2 through scattering, absorption, plasmonic sensitization and hot electron injection. The deposited TiO_2 segments are amorphous which is beneficial due to the lower electron affinity and higher hole transportation rate. The optical properties of Au/TiO_2 NRAs shows transverse and longitudinal plasmons in the visible light range which correlates closely with our theoretical predictions. Detailed XPS analysis showed that there is SBH at the interface between Au and TiO_2, which is greatly beneficial for the efficient charge separation in Au/TiO_2 NRAs. We have determined an SBH of 0.23 eV between the amorphous TiO_2 and the Au interface which is very close to the theoretical literature values. Photoelectrochemical (PEC) measurements showed 4× improved photoelectron generation in Au/TiO_2 NRAs in comparison to pristine TiO_2 NRAs, which is associated with the hot electron injection, PRET enhancement and efficient charge separation. The present results are paramount for further engineering of the 1D plasmonic Au/TiO_2 nanostructures with the desired optical properties for solar light driven applications.

Experimental details

Template-assisted electrodeposition of TiO_2 and multisegmented Au/TiO_2 NRAs into AAO membranes

We have fabricated TiO_2 and Au/TiO_2 NRAs by means of the template-assisted electrodeposition technique into AAO membranes with a pore diameter of 200 nm. The multibath electrodeposition technique allowed us to fabricate multisegmented Au/TiO_2 NRAs. For the electrodeposition of TiO_2 and Au/TiO_2 NRAs, a Cr layer ($\approx$20 nm) was first sputtered on one side of the AAO membrane to make it conductive for using it as the working electrode in a three-electrode cell. A Pt mesh electrode was used as the anode and an Ag/AgCl electrode was utilized as the reference. Au NRAs were synthesized with pulsed electrodeposition with E_{on} = −0.8 V/1 s and E_{off} = OCP/100 s by using a gold plating solution (ECOLYT SG100). For deposition of TiO_2 segments, first the pH value of the $TiCl_3$ solution was adjusted to 2.5 by addition of Na_2CO_3 solution and then the segments were deposited by employing an E_{on} = 0.8 V/1 s. In order to allow for regeneration of Ti^{3+} ion concentration at the deposition site within the AAO pores, a long pause pulse (E_{off} = OCP/100 s) was used. The number of electrodeposition cycles at each step determined the length of the segments. The number of cycles for the Au and TiO_2 segments for this study were kept at 80× and 40×, respectively.

Pristine TiO_2 and Au/TiO_2 NRAs were investigated by using scanning electron microscopy (SEM) to obtain general information about their morphology, elemental distribution and the interface properties between Au and TiO_2 segments. AAO membranes with TiO_2 and Au/TiO_2 NRAs were attached to the ITO substrate with the help of carbon tape. Free standing TiO_2 and Au/TiO_2 NRAs

were obtained by dissolving the AAO membrane with 10 M NaOH for 3 h. The sample was then washed with deionized water and absolute ethanol to completely remove the remains of the AAO membrane and dried at room temperature. The samples were investigated by field-emission SEM (FE-SEM, SUPRA 35VP, Carl Zeiss GmbH), equipped with an energy dispersive X-ray spectrometer (EDS, Oxford instruments 7059 link pentafet), allowing semi-quantitative chemical analysis.

X-ray powder diffraction (XRD) patterns of the free standing TiO_2 and Au/TiO_2 NRAs were collected on a PANanalytical X'pert PRO MPD diffractometer with Cu Kα1 radiation (1.54056 Å) in reflection geometry in the range of 10–90° in steps of 0.034°. PDF standards from the International Centre for Diffraction Data (ICDD) were used for the identification of crystalline phases.

The optical properties of free-standing TiO_2 and Au/TiO_2 NRAs were explored by utilizing UV-Vis diffuse reflectance spectrophotometry (Perkin Elmer, model Lambda 650 and Lambda 35). The reason for utilizing two different spectrophotometers was to investigate photoabsorption in two different wavelength ranges. The background correction was recorded using the white reflectance standard Spectralon©.

The TFA XPS spectrometer (Physical Electronics Inc.) was used to obtain information on elemental, surface chemical properties, and valence band maxima (VBM). The sample surfaces were excited with X-ray radiation from a monochromatic Al-Kα source (1468.6 eV). The high-energy-resolution spectra were acquired with an energy analyzer operating at a resolution of 0.06 eV and a pass energy of 29 eV. In order to reveal vital information about the valence band maxima (VBM), data were smoothed before analysis with the Savitzky–Golay (SG) filter and the method described by Chambers *et al.*[13] was used to determine the VBM position for pristine TiO_2 and Au/TiO_2 NRAs.

The PEC experiments were carried out by means of a Metrohm Autolab PGSTAT 302 potentiostat. A three-electrode configuration was employed using a screen-printed electrode (DropSens) that consists of carbon as a working electrode, platinum as a counter electrode and silver as a reference electrode. The AAO membrane was first affixed onto the working electrode with carbon tape, and the membrane was then dissolved by immersing into 10 M NaOH for 3 h. The electrode was then washed with deionized water and absolute ethanol to completely remove the remains of the AAO membrane and dried overnight at room temperature. The working electrode was either the multisegmented Au/TiO_2 NRAs or the pristine TiO_2 NRAs. The geometrical surface area of the working electrode was precisely measured with a Vernier caliper. An aqueous solution of 0.1 M KOH was used as the electrolyte. The illumination was from a 150 W Hg vapor lamp. The intensity of the illumination onto the sample surface was adjusted to 80 mW cm^{-2} using a luxmeter (PU 150). The lamp was turned on and off at an interval of 200 s.

Results and discussion

SEM and XRD analyses

Fig. 1a shows a typical SEM image of the TiO_2 NRAs embedded into the AAO membrane with a nominal pore diameter of 200 nm. SEM EDS analysis (inset of Fig. 1a) confirm that the sample consists of Ti and O without any detectable impurities. SEM images (top view) of the free standing TiO_2 NRAs after dissolving the AAO membranes are provided in Fig. 1b. The

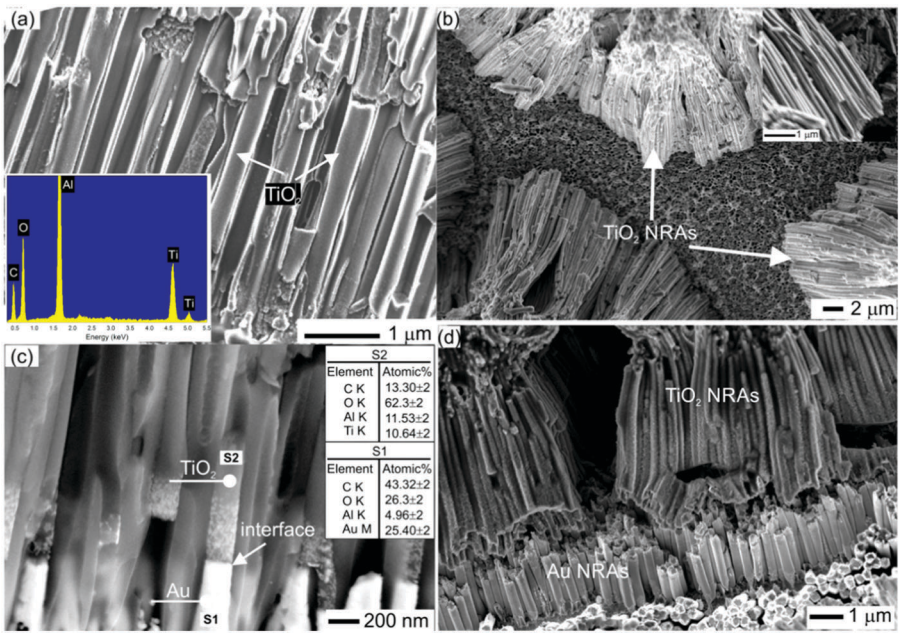

Fig. 1 (a) SEM image of the TiO_2 NRAs embedded inside the AAO membrane, inset shows SEM-EDS results of TiO_2 NRAs. (b) SEM image of the free standing TiO_2 NRAs after removing the AAO membrane (top view) (c) SEM image of the multisegmented (Au/TiO_2) NRAs embedded inside the AAO membrane (inset shows SEM-EDS results of Au and TiO_2 segments). (d) SEM image of the free standing multisegmented (Au/TiO_2) NRAs.

length of the TiO_2 NRAs is 15 μm as shown in Fig. 1b. The inset of Fig. 1b shows a close-up of a bundle of TiO_2 NRAs clearly indicating the rod-like morphology of the sample. It is clearly shown in Fig. 1c that multisegmented Au/TiO_2 NRAs were successfully fabricated. The Au (brighter) and TiO_2 (darker) segments are evident by the backscattered electron (BSE) contrast image as shown in Fig. 1c. Additionally, SEM–EDS results in Fig. 1c indicate that the segments consist of Au and TiO_2. Most importantly, the interface between Au and TiO_2 is flat and sharp as indicated by the arrow in Fig. 1c. Fig. 1d shows the multisegmented Au/TiO_2 NRAs after dissolving the AAO membrane. The Au segments have a flat surface and the length of the Au segments in Au/TiO_2 is around 1–2 μm as shown in Fig. 1c and d.

The separation between the TiO_2 and Au/TiO_2 NRAs embedded inside the AAO membrane is 356 ± 20 nm as shown in Fig. 1a and c. However, after the AAO support is dissolved, the ends of the TiO_2 rods attach to each other due to electrostatic and chemical forces, making it difficult to provide the exact separation distance between them. Careful observation of Fig. 1d reveals that the Au segments are not attached to each other and that the separation between them is 100–150 nm. It is worth mentioning that the optical (plasmonic) properties of Au/TiO_2 NRAs depend mainly on separation between Au segments (more details are in the Fig. S3, ESI†).

XRD patterns of TiO_2 and multisegmented Au/TiO_2 NRAs after dissolving the AAO membrane are presented in Fig. 2. The absence of sharp peaks of TiO_2 in the XRD pattern of both samples confirms that TiO_2 is in amorphous form.[14,15] All the diffraction peaks observed in Au/TiO_2 NRAs match exactly with the standard data of fcc Au (JCPDS 01-1174). Amorphous TiO_2 is favourable in the proposed multisegmented nanostructure because: (1) the work function of amorphous TiO_2 is lower than that of its crystalline counterpart due to the large number of oxygen vacancies.[14] (2) Amorphous TiO_2 is known to have a higher hole transfer rate,[16] so fast transportation of holes will increase the separation between charge carriers.

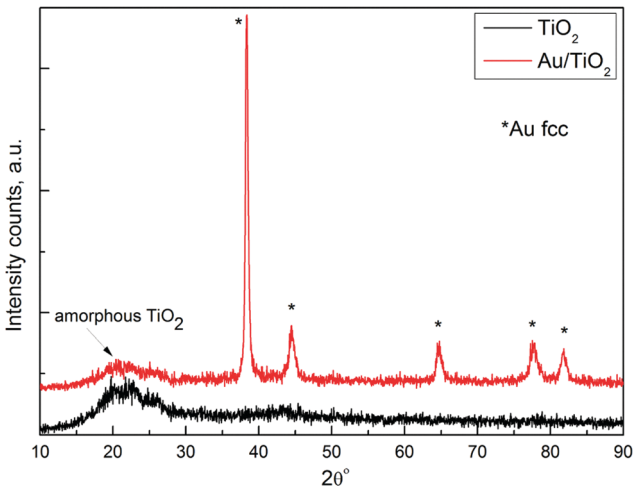

Fig. 2 XRD patterns of (a) TiO_2 and (b) Au/TiO_2 NRAs.

UV-Vis-DR analysis on free standing TiO_2 and Au/TiO_2 NRAs

Fig. 3a shows UV-Vis DR spectra for the free standing pristine TiO_2 (black line) and Au/TiO_2 (red line) NRAs. The black line shows the typical absorption behaviour associated with the TiO_2 with strong absorption in the UV-range. It can be observed that the Au/TiO_2 sample has a stronger absorption in the whole visible region as compared to the pristine TiO_2 sample.

In Au/TiO_2 NRAs the broad absorption peak around 550 nm is associated with the transverse mode (T-mode) and another hump extends to the near IR region, which can be attributed to the longitudinal mode (L-mode) of Au NRAs. These results prove that the Au/TiO_2 NRAs exhibit plasmonic behaviour under visible light irradiation. Such plasmon modes have been predicted with discrete dipole approximation (DDA) simulation.[17]

The band gaps of TiO_2 and Au/TiO_2 were determined from Tauc plots and the values are 3.62 and 3.72 eV, respectively, as shown in Fig. 3b. It is well known that amorphous TiO_2 has a larger band gap than its crystalline counterparts.[18] The observed band gap opening of Au/TiO_2 NRAs can be associated with band bending due to the charge transfer between Au and TiO_2 segments at the interface.

Fig. 3c compares the UV-Vis DR spectra of Au/TiO_2 NRAs for a larger wavelength range with DDA simulation for Au NR with an aspect ratio = 5. It is clearly seen that the T-mode perfectly matches with the simulation results; however the strong peak for the L-mode is missing. The L-mode is significantly affected by (1) change in Au segment lengths, (2) presence of titania segments and (3) the arrangement of Au NRAs, which can result in broadening and intensity loss of the L-mode. We have simulated the variation in the L-mode with the change in the aspect ratio of the Au NRs (Fig. S1, ESI†), presence of the titania segments (Fig. S2, ESI†) and the effect of the arrangement of Au NRAs (Fig. S3, ESI†). The simulation results made us conclude that the broad hump and reduced intensity of the L-mode is due to the abovementioned three factors.

The spatial distribution of the electric field (PRET) across Au/TiO_2 NRAs associated with the L-mode was obtained from DDA simulation as shown in Fig. 3d. The PRET enhancement is dominant at the extremities of Au segment, which penetrates into the TiO_2 segment for about 2 nm and creates a pathway for hot electron injection in such types of nanostructures (Fig. 3d). It is expected that the high plasmonic electric field and strong coupling between Au and TiO_2 at the interface will significantly enhance the plasmon induced charge separation, hot electron injection.[2,19]

XPS analysis of TiO_2 and Au/TiO_2

The XPS survey spectra of TiO_2 and Au/TiO_2 NRAs demonstrated that the main elements on the surface are titanium, oxygen, gold, carbon and sodium (Fig. S4, ESI†). Traces of sodium are the remains of NaOH used to dissolve the AAO membrane. No aluminium signal was detected in the full XPS spectrum (Fig. S4, ESI†) which indicates that the AAO membrane was completely dissolved. Fig. 4a–d shows the high resolution Ti 2p, O 1s, Au 4f and valence band maxima (VBM) spectra for pristine TiO_2 and

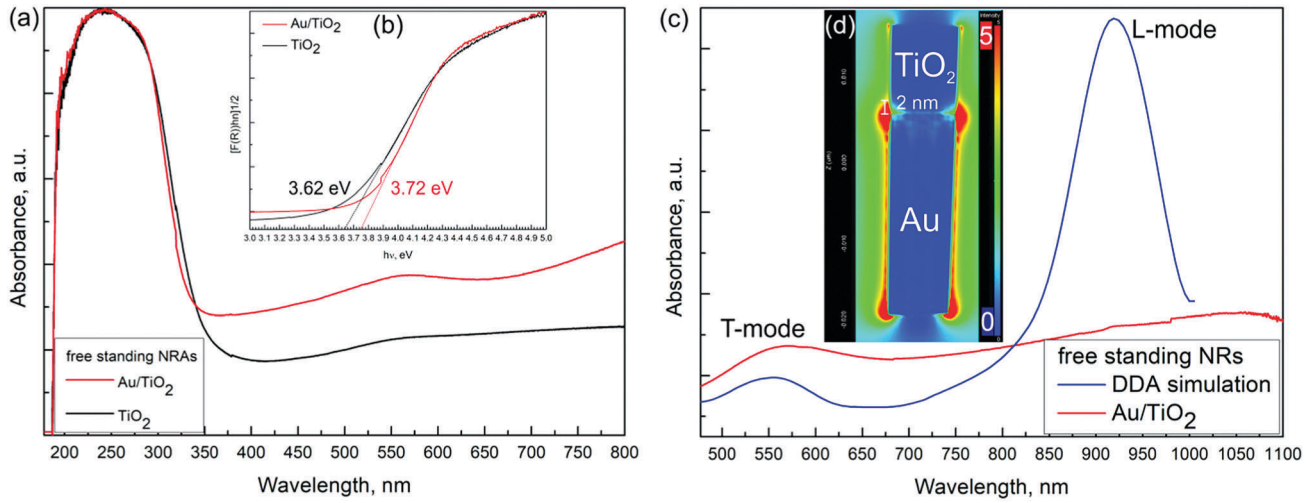

Fig. 3 (a) UV-Vis DR spectra of pure TiO_2 and Au/TiO_2 NRAs (b) Tauc plot analysis for band gap width. (c) Comparison between UV-Vis DR spectra of Au/TiO_2 and DDA simulation on Au NR. (d) Enhancement in electric field intensity for a multisegmented Au/TiO_2 NR.

Au/TiO_2 NRAs, respectively. The Ti 2p and O 1s core-level spectra of pristine TiO_2 and Au/TiO_2 NRAs look similar. According to the deconvolution results, the Ti 2p spectrum of TiO_2 and Au/TiO_2 is dominated by the Ti^{4+} species. However, the presence

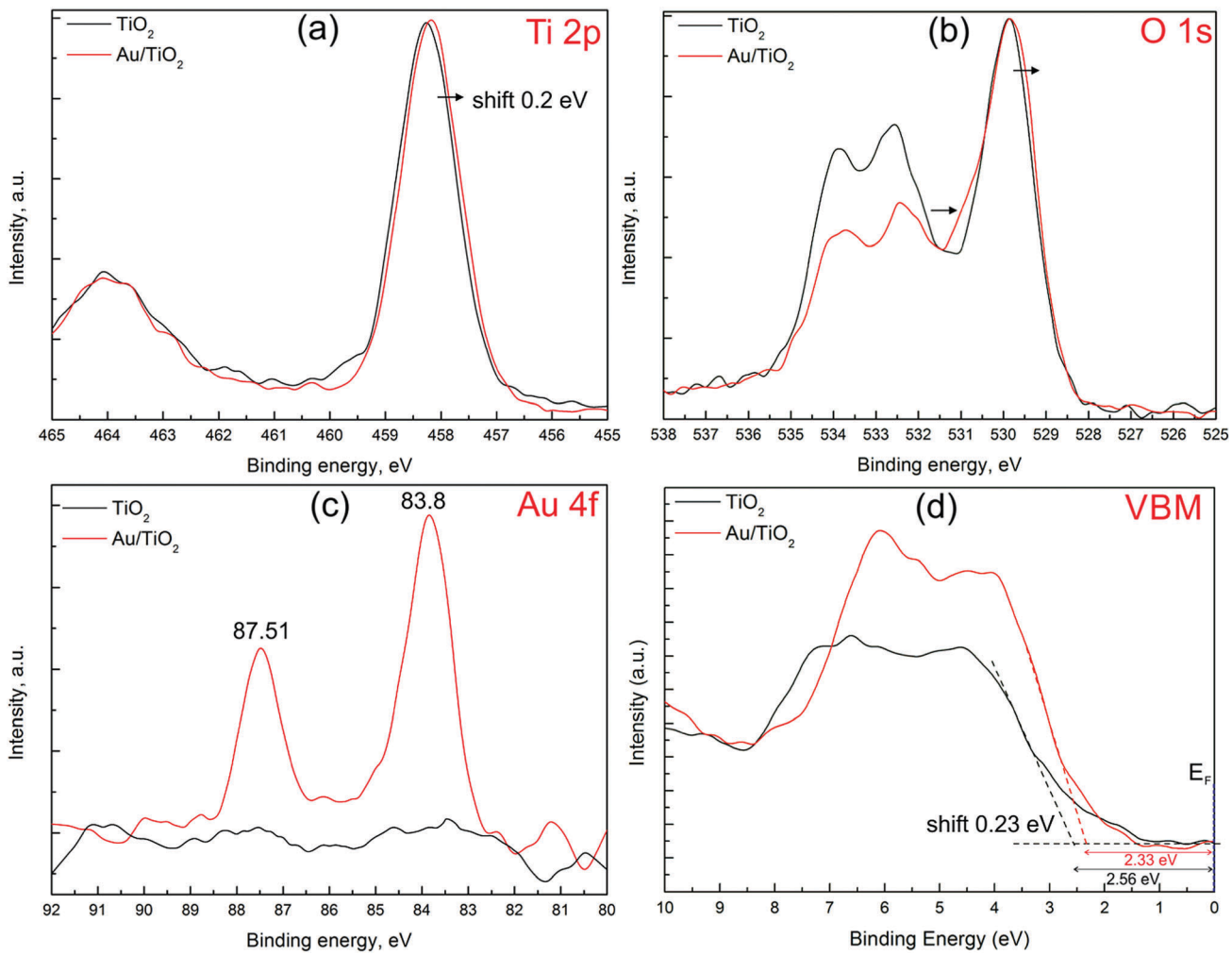

Fig. 4 XPS analysis of pure TiO_2 (black lines) and Au/TiO_2 (red lines): (a) Ti 2p, (b) O 1s, (c) Au 4f spectra and (d) determination of VBM.

of a small amount of reduced Ti^{3+} was also observed. The Ti 2p spectra for TiO_2 have Ti $2p_{1/2}$ and Ti $2p_{3/2}$ spin–orbital splitting which are located at the binding energies of 464.0 and 458.3 eV, respectively, with a difference of ~5.7 eV, typical for Ti^{4+}–O.

The O 1s spectrum (Fig. 4b) is asymmetrical for Au/TiO_2, with a tail extending towards higher energies (indicated by an arrow). A similar shape was previously observed for the Au/TiO_2 catalyst prepared by deposition–precipitation[20] and magnetron sputtering.[21] The O 1s spectra were deconvoluted into sub-peaks, the major peak is at 529.8 eV which is related with the O^{2-} oxidation state in Ti–oxide. The minor component forming the high-energy tail (shoulder) and appearing at about 0.9–1.5 eV above the major O^{2-} peak (529.9 eV) of the O 1s line was attributed to the presence of subsurface low-coordinated oxygen ions O^- (oxygen vacancies).[22,23] The relative ratio between the peak at 531.2 eV and the peak at 529.8 eV is lower for the pristine TiO_2 sample (0.22) than for the Au/TiO_2 sample (0.30) indicating that oxygen vacancies are more abundant in the Au/TiO_2 sample. Oxygen vacancies can serve as electrostatic field centers at the interface which results in adhesion between Au and TiO_2 and creates networks of Au–O–Ti.[24] The peaks at 532.4 and 533.4 eV are assigned to the single and double bonds of C–O and H_2O adsorbed on the surface of TiO_2 and Au (Fig. 4b).

Fig. 4c shows that Au exists only in the Au/TiO_2 sample, indicated by the Au $4f_{7/2}$ with a binding energy of 83.8 eV. Fitting the Au $4f_{7/2}$ spectrum of the Au/TiO_2 NRAs shows the Au segments to be in the purely metallic state.[24,25] The observed Au $4f_{7/2}$ binding energy is slightly lower than that of the bulk Au at 84.0 eV[25] which is attributed to the strong metal–semiconductor interaction. The Au segments in the Au/TiO_2 NRAs are negatively charged due to the electron transfer from oxygen vacancies in TiO_2 to achieve Fermi level equilibrium, the first indication of formation of the SBH at the interface between Au and TiO_2.[26]

The VBM results of pristine TiO_2 and Au/TiO_2 samples are shown in Fig. 4d. The VBM position for pristine TiO_2 and Au/TiO_2 with respect to the Fermi level was found to be 2.56 and 2.33 eV, respectively. Since the zero point of the binding energy scale corresponds to the Fermi level (E_F) as shown in Fig. 4d, the position of the VBMs relative to E_F show that the TiO_2 sample is n-type semiconductor. The above results indicate that the VBM of Au/TiO_2 shifts towards a lower binding energy by 0.23 eV compared to pristine TiO_2 NRAs. The VBM shift is due to the charge transfer and formation of SBH at the interface between Au and TiO_2.[5] In detail, when the TiO_2 and Au segments are coupled, the difference in work function allows the Au segments to extract and retain electrons from TiO_2.[27–29] The net charge transfer from TiO_2 to Au will continue until the Fermi levels of both materials are aligned.[5] This creates an electric field at the interface between Au and TiO_2, which is known as SBH (ϕ_{SB}). The ϕ_{SB} acts like a potential barrier for electrons moving from the Au to the TiO_2 segments and it is determined as[5,30]

$$\phi_{SB} = \phi_M - \chi \quad (1)$$

where ϕ_M = work function of Au, χ = electron affinity of the TiO_2 and ϕ_{SB} = SBH between Au and TiO_2. ϕ_{SB} in eqn (1) is equivalent to the total downward displacement of the Fermi level for the Au/TiO_2 in comparison to pristine TiO_2 NRAs as measured with XPS analysis (see Fig. 4d).[5,30,31] Thus, in our case the value of ϕ_{SB} is 0.23 ± 0.03 eV which is consistent with the theoretical reported values between Au and TiO_2.[32,33] In the pioneering work of McFarland and Tang[34] on the Au/TiO_2(110) interface, they found ϕ_{SB} equal to 0.9 eV. However, later Ivan and Stefano[32] showed that the value of ϕ_{SB} is strongly affected by oxygen vacancies in the TiO_2 structure. They further observed that the value of ϕ_{SB} can be as low as 0.15 eV for substoichiometric TiO_2 in the Au/TiO_2 composite. As mentioned previously, amorphous TiO_2 has more oxygen vacancies as compared to its crystalline counterparts,[16] which results in a lower value of ϕ_{SB} = 0.23 ± 0.03 eV. Additionally, reduced SBH (ϕ_{SB}) would be favourable for the propagation and migration of electrons through the metal–semiconductor interface.

Photoelectrochemical measurements of TiO_2 and Au/TiO_2

We further studied the PEC measurements in a three electrode cell arrangement on pristine TiO_2 and multisegmented Au/TiO_2 NRAs. Upon light excitation, the photocurrent responses of TiO_2 (black line) and Au/TiO_2 (red line) were obtained as shown in Fig. 5. The TiO_2 NRAs exhibit a photocurrent density of 15 μA cm^{-2}, however, the photocurrent density of the multi-segmented Au/TiO_2 NRAs is around 50 μA cm^{-2}. During the repeated ON/OFF switching, after the first few pulses no significant photocurrent density degradation was observed for pristine TiO_2 as well as Au/TiO_2 NRAs, which reveals the good reversibility of the process and photostability of the samples. The photocurrent behaviour can be influenced by many factors including the plasmon damping process,[35] hot electron generation[36] and plasmon induced charge transfer mechanisms.[37,38]

The photocurrent density of Au/TiO_2 NRAs is 4 times larger than that of the pristine TiO_2, which can be associated with the plasmon-sensitized process *via* hot electron injection and PRET

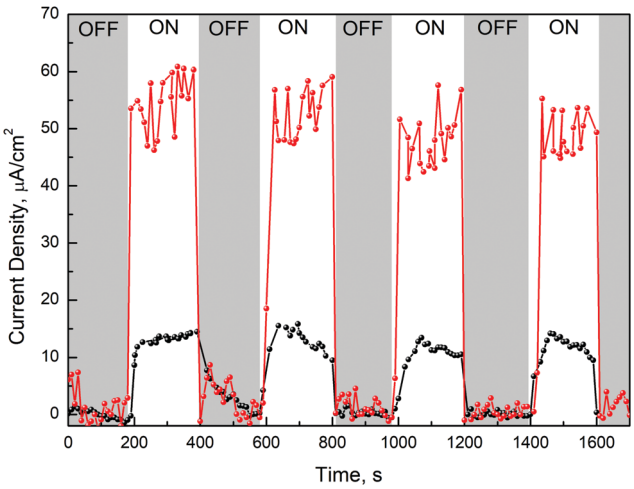

Fig. 5 Photoinduced current measurements on pure TiO_2 NRAs (black line) and multisegmented Au/TiO_2 NRAs (red line) with and without light excitations.

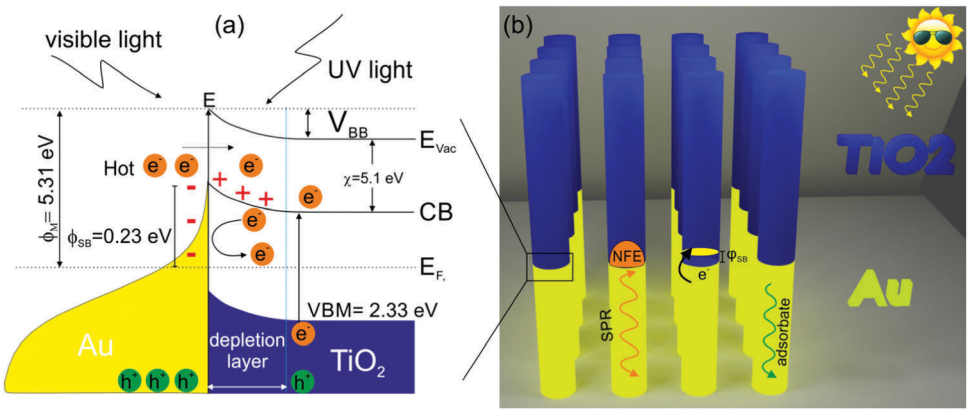

Fig. 6 (a) Band diagram of the Au/TiO_2 system, the optical process, hot electron injection, generation of SBH at the interface. (b) Schematic image of the free standing multisegmented (Au/TiO_2) NRAs.

enhancement from Au to TiO_2 segments. Therefore, the synergistic effect of the local PRET enhancement (Fig. 3d) and the hot electron injection significantly increases the electron/hole pair generation in Au/TiO_2 NRAs. In addition, the SPR wavelength of Au is above 500 nm (Fig. 3a), therefore the enhancement of the photo-absorption and generation of hot electrons in Au/TiO_2 NRAs is in the visible and NIR light ranges. The above-mentioned results of multisegmented Au/TiO_2 NRAs can be well understood by the formation of SBH and by taking into account the hot electron transfer model as shown in Fig. 6a. After contacting Au and TiO_2 as shown in Fig. 6b, electrons are extracted from TiO_2 to the contiguous Au segment in order to maintain the Fermi level equilibrium. The literature value of the work function of Au is 5.31 eV[39] and the TiO_2 electron affinity is around 4.9–5.1 eV.[40] Thus, as a result of the Fermi level equilibrium, a SBH of about 0.23 eV is generated at the Au/TiO_2 interface as was observed in the XPS spectra of VBM (Fig. 4d). The hot electrons generated in Au have an energy of around 1–2 eV,[41–43] thus ensuring that the hot electrons generated in the SPR process will flow across the SBH and result in a high photocurrent density as shown in Fig. 5. In addition, amorphous TiO_2 possesses absorption in the UV light region, and a great amount of electron–hole pairs can be generated in the TiO_2 segment under UV-light irradiation, which contributes also as photoelectrons. There are some theoretical and experimental reports on hot electron injection and PRET enhancement between Au and TiO_2 nanostructures.[35,36,44,45] However, this work is important as it provides both theoretical as well as experimental results on novel immobilized multisegmented Au/TiO_2 NRAs to investigate the enhanced photocurrent due to the plasmonic-induced hot electron injection and to explain their potential for future solar-light induced photocatalysis.

Conclusions

We have fabricated immobilized multisegmented Au/TiO_2 NRAs inside AAO membranes *via* a template-assisted electro-deposition technique. UV-Vis DR measurements on free standing Au/TiO_2 NRAs showed a broad spectrum at 550 nm which is ascribed to the T-mode. It was shown with the simulation results that the intensity of the L-mode was reduced due to three factors namely, (1) size variation of the Au NRs, (2) presence of the TiO_2 segment, and (3) hexagonally arranged Au arrays. Taking into consideration these experimental factors, the UV-Vis results are in good correlation with simulation data. The band gap opening for Au/TiO_2 NRAs is attributed to the formation of the SBH, which is subsequently related to the charge transfer between Au and TiO_2 at the interface. The XPS results showed reduced binding energy for Au $4f_{7/2}$ and concurrent increase in the Ti^{3+}–O species, which is considered as direct evidence for charge transfer from oxygen vacancies in TiO_2 to Au segments. Detailed XPS analysis on VBM allowed us to determine an SBH of 0.23 ± 0.03 eV between the amorphous TiO_2 and the Au interface, which is very close to theoretical literature values. The generation of photo-electrons in Au/TiO_2 NRAs is 4× higher than pristine TiO_2 NRAs, which is associated with the plasmon-sensitized process *via* hot electron injection, PRET enhancement from Au to TiO_2 segments and charge carriers generated *via* the UV-light absorption in TiO_2. Our study directly probes the SBH and enhanced photoelectron generation in novel plasmonic immobilized multisegmented Au/TiO_2 NRAs. Further improvements in photocurrent output can be achieved through the optimization of Au/TiO_2 architecture and interface engineering. Such nano-structural Au/TiO_2 NRAs have potential applications for efficient solar energy harvesting devices.

Conflicts of interest

There are no conflicts to declare.

Acknowledgements

The authors acknowledge financial support from the Slovenian Research Agency (research core funding No. P2-0150). M. S. Arshad also acknowledges the help of Irena Abramovič for the electrodeposition of Au/TiO_2 NRAs, Dr Gregor Žerjav for help regarding PEC measurements and Tatjana Filipič for help with XPS characterization.

References

1 Z. Xuming, C. Yu Lim, L. Ru-Shi and T. Din Ping, *Rep. Prog. Phys.*, 2013, **76**, 046401.
2 X.-C. Ma, Y. Dai, L. Yu and B.-B. Huang, *Light: Sci. Appl.*, 2016, **5**, e16017.
3 W. Hou and S. B. Cronin, *Adv. Funct. Mater.*, 2013, **23**, 1612–1619.
4 M. R. Khan, T. W. Chuan, A. Yousuf, M. N. K. Chowdhury and C. K. Cheng, *Catal. Sci. Technol.*, 2015, **5**, 2522–2531.
5 Z. Zhang and J. T. Yates, *Chem. Rev.*, 2012, **112**, 5520–5551.
6 K. Horn, *Appl. Phys. A: Mater. Sci. Process.*, 1990, **51**, 289–304.
7 Y. Gao, *Mater. Sci. Eng., R*, 2010, **68**, 39–87.
8 L. Wen, Z. Wang, Y. Mi, R. Xu, S.-H. Yu and Y. Lei, *Small*, 2015, **11**, 3408–3428.
9 Y. J. Hwang, A. Boukai and P. Yang, *Nano Lett.*, 2009, **9**, 410–415.
10 L. J. Lauhon, M. S. Gudiksen, D. Wang and C. M. Lieber, *Nature*, 2002, **420**, 57–61.
11 A. W. Maijenburg, E. J. B. Rodijk, M. G. Maas, M. Enculescu, D. H. A. Blank and J. E. ten Elshof, *Small*, 2011, **7**, 2709–2713.
12 Y. Xia, P. Yang, Y. Sun, Y. Wu, B. Mayers, B. Gates, Y. Yin, F. Kim and H. Yan, *Adv. Mater.*, 2003, **15**, 353–389.
13 S. A. Chambers, T. Droubay, T. C. Kaspar and M. Gutowski, *J. Vac. Sci. Technol., B: Microelectron. Nanometer Struct.–Process., Meas., Phenom.*, 2004, **22**, 2205–2215.
14 B. Bharti, S. Kumar, H.-N. Lee and R. Kumar, *Sci. Rep.*, 2016, **6**, 32355.
15 B. Bharti, S. Kumar and R. Kumar, *Appl. Surf. Sci.*, 2016, **364**, 51–60.
16 H. H. Pham and L.-W. Wang, *Phys. Chem. Chem. Phys.*, 2015, **17**, 541–550.
17 P. K. Jain, X. Huang, I. H. El-Sayed and M. A. El-Sayed, *Plasmonics*, 2007, **2**, 107–118.
18 K. Kaur and C. V. Singh, *Energy Procedia*, 2012, **29**, 291–299.
19 Y.-C. Yen, J.-A. Chen, S. Ou, Y.-S. Chen and K.-J. Lin, *Sci. Rep.*, 2017, **7**, 42524.
20 B. Schumacher, V. Plzak, J. Cai and R. J. Behm, *Catal. Lett.*, 2005, **101**, 215–224.
21 G. M. Veith, A. R. Lupini and N. J. Dudney, *J. Phys. Chem. C*, 2009, **113**, 269–280.
22 J.-C. Dupin, D. Gonbeau, P. Vinatier and A. Levasseur, *Phys. Chem. Chem. Phys.*, 2000, **2**, 1319–1324.
23 H. Liu, W. Yang, Y. Ma, Y. Cao, J. Yao, J. Zhang and T. Hu, *Langmuir*, 2003, **19**, 3001–3005.
24 H. Chen, P. Li, N. Umezawa, H. Abe, J. Ye, K. Shiraishi, A. Ohta and S. Miyazaki, *J. Phys. Chem. C*, 2016, **120**, 5549–5556.
25 N. Kruse and S. Chenakin, *Appl. Catal., A*, 2011, **391**, 367–376.
26 V. Jovic, W.-T. Chen, D. Sun-Waterhouse, M. G. Blackford, H. Idriss and G. I. N. Waterhouse, *J. Catal.*, 2013, **305**, 307–317.
27 H. B. Michaelson, *J. Appl. Phys.*, 1977, **48**, 4729–4733.
28 A. Borodin and M. Reichling, *Phys. Chem. Chem. Phys.*, 2011, **13**, 15442–15447.
29 N. T. Khoa, S. W. Kim, D.-H. Yoo, E. J. Kim and S. H. Hahn, *Appl. Catal., A*, 2014, **469**, 159–164.
30 R. T. Tung, *Appl. Phys. Rev.*, 2014, **1**, 011304.
31 D. Zhang, M. Yang, H. Gao and S. Dong, *J. Phys. Chem. C*, 2017, **121**, 7139–7143.
32 I. Marri and S. Ossicini, *Solid State Commun.*, 2008, **147**, 205–207.
33 Y. Jiao, A. Hellman, Y. Fang, S. Gao and M. Käll, *Sci. Rep.*, 2015, **5**, 11374.
34 E. W. McFarland and J. Tang, *Nature*, 2003, **421**, 616–618.
35 M. L. Brongersma, N. J. Halas and P. Nordlander, *Nat. Nanotechnol.*, 2015, **10**, 25–34.
36 A. Manjavacas, J. G. Liu, V. Kulkarni and P. Nordlander, *ACS Nano*, 2014, **8**, 7630–7638.
37 C. Boerigter, U. Aslam and S. Linic, *ACS Nano*, 2016, **10**, 6108–6115.
38 C. Boerigter, R. Campana, M. Morabito and S. Linic, *Nat. Commun.*, 2016, **7**, 10545.
39 J. Rumble, *CRC Handbook of Chemistry and Physics*, Taylor & Francis, 98th edn, 2006.
40 D. O. Scanlon, C. W. Dunnill, J. Buckeridge, S. A. Shevlin, A. J. Logsdail, S. M. Woodley, C. R. A. Catlow, M. J. Powell, R. G. Palgrave, I. P. Parkin, G. W. Watson, T. W. Keal, P. Sherwood, A. Walsh and A. A. Sokol, *Nat. Mater.*, 2013, **12**, 798–801.
41 S. M. Sze, J. L. Moll and T. Sugano, *Solid-State Electron.*, 1964, **7**, 509–523.
42 L. Young Keun, L. Hyosun, L. Changhwan, H. Euyheon and P. Jeong Young, *J. Phys.: Condens. Matter*, 2016, **28**, 254006.
43 J. R. M. Saavedra, A. Asenjo-Garcia and F. J. García de Abajo, *ACS Photonics*, 2016, **3**, 1637–1646.
44 S. Linic, P. Christopher and D. B. Ingram, *Nat. Mater.*, 2011, **10**, 911–921.
45 M. Wang, M. Ye, J. Iocozzia, C. Lin and Z. Lin, *Adv. Sci.*, 2016, **3**, 1600024.

